cladistic hypotheses. Even in the 15% of cases in which cladistics outperformed stratocladistics, the closest topology was, on average, hidden among 227.5 topologies, compared with 1.4 for stratocladistics. Comparisons of average and minimum CFIs (Fig. 2, B and C) favor stratocladistics even more strongly.

To examine the relation between the variables in our study and values of CFI_{max}, we grouped the data in Fig. 2A by percent OTU-loss and by F and B (Tables 1 and 2). Each group of results was subjected to a sign test to determine if CFI_{max} was significantly higher for one method or the other (*18*). In most cases, mean CFI_{max} is higher for stratocladistics and the sign tests are highly significant ($P < 0.001$) in favor of stratocladistics. In three cases, mean CFI_{max} is higher for cladistics, but the differences from CFI_{max} for stratocladistics are not significant. Of the remaining six sign tests that were not significant, only one (OTU-loss = 80%) did not have more cases with higher stratocladistic CFI_{max} than cladistic CFI_{max}. Thus, stratocladistics generally outperforms cladistics to a statistically significant degree, and this outcome is largely independent of the evolutionary model and completeness of the fossil record assumed.

Our results lay to rest the notion that an incomplete fossil record yields no clues for inferring phylogeny. The stratigraphic order of taxa preserved in the fossil record is a complex function of presence and absence controlled by many physical, chemical, and biological factors. To ignore this pattern or dismiss this class of data when it does not agree with a phylogenetic hypothesis makes an unwarranted "covering assumption" (*5*) that masks the real weight-of-evidence and encourages less than even-handed treatment of data. Stratocladistic hypotheses attempt to explain both the distribution of characters among taxa and the distribution of taxa through time. By doing this, stratocladistic hypotheses explain more features of the natural world and hence have greater explanatory power than purely cladistic hypotheses.

References and Notes

1. D. L. Hull, *Science as a Process* (Univ. of Chicago Press, Chicago, IL, 1988); E. Sober, *Reconstructing the Past: Parsimony, Evolution and Inference* (MIT Press, Cambridge, MA, 1988).
2. A. B. Smith, *Systematics and the Fossil Record* (Blackwell, London, 1984). See also *Nature* Debates [online] (19 November 1998) at http://helix.nature.com/debates/index.html.
3. B. Schaeffer, M. K. Hecht, N. Eldredge, in *Evolutionary Biology*, T. Dobzhansky, M. Hecht, W. C. Steere, Eds. (Appleton-Century-Crofts, New York, 1972), vol. 6, chap. 2.; G. Nelson, *Syst. Zool.* **27**, 324 (1978).
4. E. O. Wiley, *Phylogenetics: The Theory and Practice of Phylogenetic Systematics* (Wiley, New York, 1981).
5. J. S. Farris, in *Advances in Cladistics*, N. J. Platnick and V. A. Funk, Eds. (Columbia Univ. Press, New York, 1983), vol. 2, pp. 7–36.
6. D. C. Fisher, in W. P. Maddison and D. R. Maddison, *MacClade, ver. 3.0* (Sinauer, Sunderland, MA, 1992), pp. 124–129; D. C. Fisher, in *Interpreting the Hierarchy of Nature*, L. Grande and O. Rieppel, Eds. (Academic Press, New York, 1994), pp. 133–172; P. D. Polly, *Contrib. Mus. Paleontol. Univ. Mich.* **30**, 1 (1997).
7. Cladograms represent only the relative recency of ancestry of the ingroup taxa and not explicit phylogenetic relationships. A given cladogram is consistent with multiple phylogenetic trees, which express explicit relationships between ingroup taxa, either as sister taxa with a hypothetical ancestor or as ancestor-descendant pairs [N. Eldredge and J. Cracraft, *Phylogenetic Patterns and the Evolutionary Process* (Columbia Univ. Press, New York, 1980); G. Nelson and N. I. Platnick, *Systematics and Biogeography: Cladistics and Vicariance* (Columbia Univ. Press, New York, 1981)].
8. Fractional OTUs are not deleted; for example, 70% of 31 OTUs is 21.7 OTUs, but only 21 are deleted.
9. Outgroups implicitly polarize character change, rooting the unrooted networks selected by parsimony [W. P Maddison, M. J. Donoghue, D. R. Maddison, *Syst. Zool*. **33**, 83 (1984); P. H. Weston, in *Models in Phylogeny Reconstruction*, R. W. Scotland, D. J. Siebert, D. M. Williams, Eds. (Clarendon, Oxford, 1994), pp. 125–155].
10. Most simulated lineages persist through multiple time intervals. Our complete, seven (plus) lineage histories thus include more than seven lineage segments, or OTUs.
11. D. L. Swofford, *Phylogenetic Analysis Using Parsimony (PAUP), ver. 3.1.1* (Illinois Natural History Survey, Champaign, IL, 1991).
12. W. P. Maddison and D. R. Maddison, *MacClade, ver. 3.0* (Sinauer, Sunderland, MA, 1992).
13. M. Foote and D. M. Raup, *Paleobiology* **22**, 121 (1996); C. R. C. Paul, in *The Adequacy of the Fossil Record*, S. K. Donovan and C. R. C. Paul, Eds. (Wiley, Chichester, UK, 1998), pp. 1–22.
14. Occasional branch and bound checks on matrices small enough to analyze with that algorithm suggest that for the simulated data, 50 replicates of the heuristic search were adequate. However, given our results, using only 50 replicates is not a liability to cladistics. Because the true cladograms are generally less parsimonious than the associated sets of cladistic results, it is unlikely that even shorter cladograms would be closer topologically to the true cladogram.
15. All intervals are equally weighted, although sedimentological, lithological, and taphonomic data could, in principle, be used to weight the stratigraphic character differentially for specific intervals or lineage segments.
16. RI is a measure of the homoplasy implied by a hypothesis for given character data and ranges from 0 for worst fit to 1 for best [J. S. Farris, *Cladistics* **5**, 417 (1989)]. Published RIs are from W. C. Clyde and D. C. Fisher [*Paleobiology* **23**, 1 (1996)] and all volumes of *Palaeontology*, *Journal of Paleontology*, and *Journal of Vertebrate Paleontology* from 1994 to 1998.
17. Subclades are the proper subsets of a whole cladogram. The whole cladogram does not count as a subclade. The number of subclades is equivalent to the number of internal nodes. The consensus fork index is simply the number of subclades (or internal nodes) shared between cladograms being compared, divided by the total number of subclades.
18. The sign test calculates the probability that the sign of the difference between stratocladistic and cladistic CFI_{max} for each grouping is equally distributed between positive and negative.

19. We thank T. K. Baumiller, J. I. Bloch, W. C. Clyde, P. D. Gingerich, and M. D. Uhen for helpful comments during the development of this project and manuscript.

29 December 1998; accepted 9 March 1999

Two-Dimensional Photonic Band-Gap Defect Mode Laser

O. Painter,[1] R. K. Lee,[1] A. Scherer,[1]* A. Yariv,[1] J. D. O'Brien,[2] P. D. Dapkus,[2] I. Kim[2]

A laser cavity formed from a single defect in a two-dimensional photonic crystal is demonstrated. The optical microcavity consists of a half wavelength–thick waveguide for vertical confinement and a two-dimensional photonic crystal mirror for lateral localization. A defect in the photonic crystal is introduced to trap photons inside a volume of 2.5 cubic half-wavelengths, approximately 0.03 cubic micrometers. The laser is fabricated in the indium gallium arsenic phosphide material system, and optical gain is provided by strained quantum wells designed for a peak emission wavelength of 1.55 micrometers at room temperature. Pulsed lasing action has been observed at a wavelength of 1.5 micrometers from optically pumped devices with a substrate temperature of 143 kelvin.

In 1946, Edward Purcell (*1*) first proposed that the spontaneous emission from an excited state of an atom can be significantly altered by placing it in a low-loss cavity with dimensions on the order of the electromagnetic wavelength. More recently, with the advent of the semiconductor laser and the improvement in crystal growth and fabrication technology, there has been increasing interest in the engineering of optical microcavities in semiconductors for spontaneous emission control (*2*–*4*). The vertical cavity surface emitting laser (*5*) (VCSEL), in which light is confined between two epitaxially grown distributed Bragg reflectors, was one of the first semiconductor cavities with dimensions on the order of the wavelength of light. Another microcavity laser, the microdisk laser (*6*), uses total internal reflection at the edge of a high refractive index disk to

[1]Departments of Electrical Engineering and Applied Physics, California Institute of Technology, Pasadena, CA 91125, USA. [2]Department of Electrical Engineering, University of Southern California, Los Angeles, CA 90089, USA.

*To whom correspondence should be addressed. E-mail: etcher@cco.caltech.edu

form low-loss whispering gallery–type modes. We describe initial experimental results of a type of microcavity laser in which light is confined to a single defect of a nanofabricated two-dimensional (2D) photonic crystal (*7*). The ability to fabricate compact lateral microcavities is important for the construction of high-density multiwavelength optical circuits. The advantage of using a photonic crystal is the inherent flexibility in geometry which allows fine-tuning of the defect mode radiation pattern (*8*) as well as the emission wavelength. The compact size and high spontaneous emission coupling factor (β) of the defect microcavity (*9*) also make it interesting as a low-noise (*3*), low-threshold (*10*) light source. In addition, microcavities based upon nanofabricated photonic crystals may be useful where crystal growth of high-index contrast mirrors are limited, such as in long-wavelength VCSELs or blue-green gallium nitride–based devices (*11*).

In the defect cavity (Fig. 1), light is contained inside the microcavity by two different mechanisms. First, a λ/2 high-index slab is used to trap photons in the vertical direction by way of total internal reflection (TIR) at the air-slab interface. Second, the light is localized in-plane, using a fabricated 2D photonic crystal consisting of a hexagonal array of air holes etched into the slab. The periodic variation in the refractive index gives rise to Bragg scattering of photons, which opens up forbidden energy gaps in the in-plane photon dispersion relation (*7*). The photonic crystal thus provides an energy barrier for the propagation of guided electromagnetic waves with frequencies that lie within the band gap. In the simplest structure, a single hole is removed in the photonic crystal, similar to a phase-slip in a distributed feedback laser, thus forming a resonant cavity. The resonant mode is highly localized to the defect region, and photons can only escape by either tunneling through the 2D photonic crystal or by impinging on the air-slab interface at a sufficiently high angle to leak out in the vertical direction.

The defect laser cavities were fabricated in indium gallium arsenic phosphide (InGaAsP). The low nonradiative surface recombination rate of this material and its relatively long emission wavelength (1.5 μm) make it a good candidate for photonic crystal microcavities (*12*). Metalorganic chemical vapor deposition (MOCVD) was used to grow the laser structure on an indium phosphide (InP) substrate. The active region consisted of four 9-nm 0.85% compressively strained InGaAsP quantum wells (QWs) separated by 20-nm quaternary barriers with a 1.22-μm band gap (*13, 14*). The QW emission wavelength is designed for 1.55 μm at room temperature, and because of the compressive strain, the coupling is strongest to photons with in-plane (transverse) electric field polarizations (TE). This is desirable because the defect mode is predominantly TE polarized in the active region.

The fabrication of the defect cavity required a number of dry etching steps followed by a wet etch to free the QW active region from the substrate. The 2D photonic crystal was patterned using electron-beam lithography on a modified Hitachi S4500-II field-emission microscope. An argon ion-beam etch was used to transfer the 2D pattern from the electron-beam resist into a metal mask layer, followed by a reactive-ion etch to transfer the pattern into a silicon nitride mask layer. The 2D photonic crystal was then etched into the InGaAsP using a Cl_2-assisted ion-beam etch. This resulted in air holes that penetrate through the active region and into an underlying sacrificial InP layer. The sample was then dipped into a diluted $HCl:H_2O$ (4:1) solution at 1°C, which selectively etched away the InP layer, leaving a free-standing membrane (Fig. 1). A scanning electron microscope (SEM) micrograph shows a top view of the fabricated microcavity (Fig. 2).

The localized defect modes of the hexagonal lattice have been studied in two dimensions (*15*), where the photonic crystal is infinite in the third dimension. More recently (*8, 16, 17*), the properties of the defect modes of a photonic crystal embedded in an optically thin waveguide were analyzed using 3D finite-difference time-domain (FDTD) calculations. The important parameters in determining the properties of the optical cavity are the refractive index n_{slab} of the dielectric slab, the thickness of the slab d, the interhole spacing a, and the radius r of the air holes.

The defect modes formed by removing a single hole are a pair of degenerate dipole modes. In the laser cavity studied here, the symmetry of the cavity was lowered by increasing the radius of two nearest-neighbor holes along the $\hat{x}$ direction (Fig. 2). This resulted in a single mode optical cavity (*8*), in which only the y-dipole mode is well localized. The magnitude of the electric field of the y-dipole mode, calculated using FDTD, was plotted (Fig. 3). The polarization of this mode is predominantly TE inside the high-

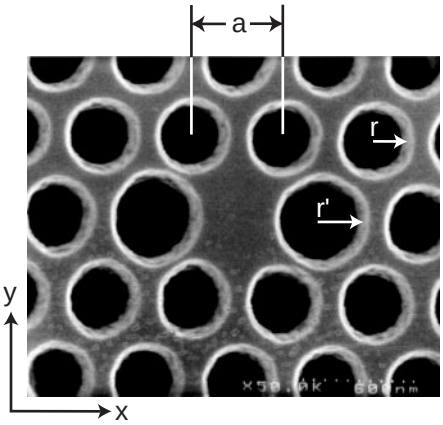

Fig. 2. Top view of a microfabricated 2D hexagonal array of air holes in a thin membrane with a central hole missing. The interhole spacing (a) is 515 nm, and the radius of the holes (r) is ~180 nm. The two enlarged holes, which are used to split the dipole mode degeneracy, have a radius (r′) of 240 nm. The InGaAsP membrane is 220 nm (half-wavelength) in thickness. Dotted line at the bottom right indicates a length of 600 nm.

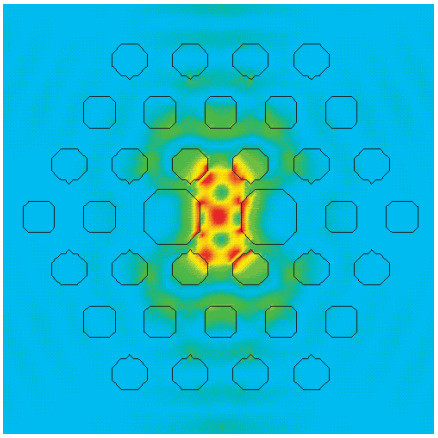

Fig. 3. A 2D slice through the middle of the slab shows the electric field amplitude of the y-dipole mode. The defect mode has a large overlap with the gain region due to the antinode at the center of the defect. The enlarged air holes serve two functions: the first is to tune the y-dipole mode frequency so as to maximize the Q, and the second is to push the x-dipole mode frequency out of the band gap of the photonic crystal, resulting in a single-mode cavity.

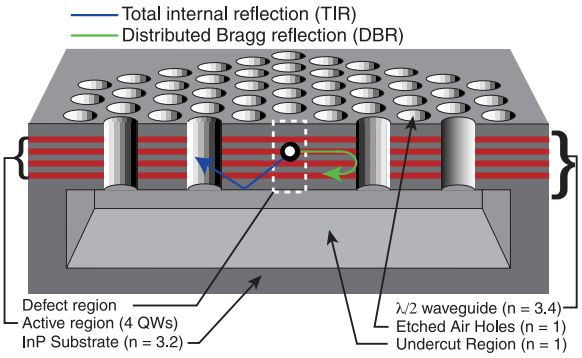

Fig. 1. Cross section through the middle of the photonic crystal microcavity. A defect is formed in the 2D photonic crystal by removing a single hole, thus forming an energy well for photons similar to that for electrons in a quantum wire structure. Photons are also localized vertically by TIR at the air-slab interface. The combination of Bragg reflection from the 2D photonic crystal and TIR from the low-index cladding (air) results in a three-dimensionally confined optical mode.

index slab. The dimensions of the laser cavity (as measured from the SEM micrograph) are a = 515 nm, r = 180 nm, r' = 240 nm, and d = 210 nm, where r' is the radius of the enlarged holes used to split the dipole mode degeneracy. Simulations of this cavity, with n_{slab} = 3.4, give an estimate of 250 for the quality factor (Q) and a normalized frequency a/λ_o of 0.34 for the y-dipole mode. The effective modal volume can be defined (*16*) in terms of the electrical field energy density in the cavity as follows

$$V_{mode}^{eff} \equiv \frac{\int_V \epsilon(\vec{r})|\vec{E}(\vec{r})|^2 d^3r}{\max[\epsilon(\vec{r})|\vec{E}(\vec{r})|^2]}$$

The y-dipole mode has an effective modal volume of 2.5 cubic half-wavelengths [$2.5(\lambda/2n_{slab})^3$]. For a lattice spacing of 515 nm, the above normalized values correspond to a resonance peak wavelength of 1509 nm and a modal volume of 0.03 μm^3. Simulations of the radiation pattern of the y-dipole mode show that nearly all the power is emitted vertically for the cavity geometry of the laser we studied. This is due to the large number of periods of the photonic crystal surrounding the defect region and the rather large r/a ratio in the actual fabricated structure (*8*). The in-plane band gap (for TE-like modes) of the photonic crystal extends over a normalized frequency range of 0.296 to 0.408, or 1.25 to 1.72 μm, assuming a wavelength of the y-dipole mode of 1.5 μm.

The laser structures were optically pumped with a semiconductor laser of 830 nm wavelength, focused to a spot size of ~3 μm on the sample surface. A microscope objective was used to focus the pump beam as well as to collect the photoluminescence from the top side of the sample. Alignment of the pump beam to the desired defect cavity was done by imaging the front sample surface using a white-light source. The fabricated microcavities have eight periods of the photonic crystal surrounding the defect, resulting in an undercut region of ~8 μm in diameter. The cavity mode, by comparison, is <0.5 μm in diameter. Pulsed lasing action was observed at a substrate temperature of 143 K with pulses of 10 ns (250 ns period). A spectrum of the laser line above threshold is shown (Fig. 4) where the lasing wavelength is 1504 nm, very close to the predicted value for the y-dipole mode. The spontaneous emission well below threshold (Fig. 4, inset) is a combination of emission from the defect cavity and emission from the surrounding unprocessed area excited by the tail of the pump beam. The broad shorter wavelength peak at 1460 nm (blue-shifted because of the lower temperature of the substrate) corresponds to emission from unprocessed material surrounding the defect cavity. The narrow longer wavelength peak is the defect mode resonance. The emission from the undercut microcavity, which is at a higher temperature than the substrate, is red-shifted and much broader, as evident by the long wavelength tail in the emission spectra. The linewidth of the defect laser narrows dramatically from 7 nm (Q = 250) below threshold to 2 Å above threshold (resolution limited). An L-L (light-out versus light-in) curve of the collected power at the lasing wavelength versus pump power (Fig. 5) shows an external threshold pump power of 6.75 mW.

The large threshold pump power is a result of the low Q value (250) of the defect mode, poor thermal heat-sinking of the floating membrane, and inefficient optical pumping (the pump beam is more than 30 times larger in area than the defect mode itself). The structure in the L-L plot near threshold may be due to the complex interplay between nonradiative and radiative processes as temperature and the stimulated emission rate change. Also, although this microcavity theoretically has a near unity β value (*9*), the L-L plot shows a distinct slope change at threshold. This may be due, in part, to the relatively high temperature of the undercut membrane and high carrier density near threshold, which results in a much larger nonradiative Auger recombination rate and subsequent low radiative efficiency below threshold. The laser cavity we describe is not optimal, however, and by tailoring the ratio of r/a and r'/a, the Q can theoretically be increased above 1500, which would significantly lower pump threshold values and increase the device operating temperature. In larger 2D photonic crystal microcavities with active regions 12 μm in diameter and correspondingly higher Q values (*18*), we obtained pulsed, room-temperature lasing. Continuous operation at room temperature for both the defect cavities and the larger structures will ultimately require better heat sinking of the membrane (*19, 20*).

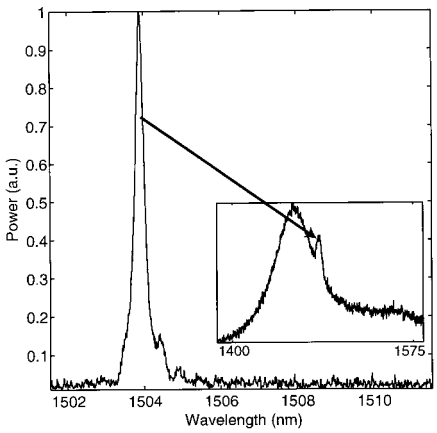

Fig. 4. Spectrum of the laser line just above threshold. The linewidth is ~0.2 nm, limited by the resolution of the spectrometer. The spontaneous emission well below threshold is shown in the inset; a.u., arbitrary units.

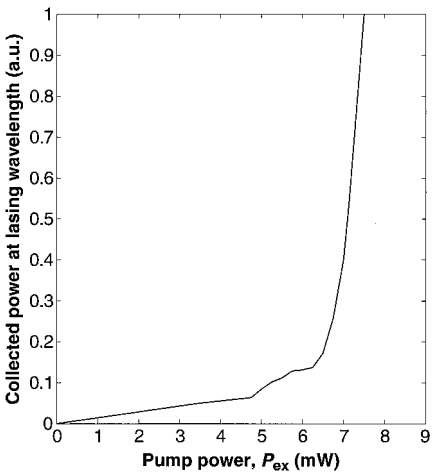

Fig. 5. L-L curve showing the power at the laser wavelength versus the incident pump power. The sample was cooled to 143 K and pumped with 10-ns pulses (4% duty cycle). The actual absorbed pump power is difficult to estimate for a structure with this geometry.

References and Notes

1. E. M. Purcell, *Phys. Rev.* **69**, 681 (1946).
2. E. Yablonovitch, *Phys. Rev. Lett.* **58**, 2059 (1987).
3. Y. Yamamoto and S. Machida, *Phys. Rev. A* **44**, 657 (1991).
4. T. Erdogan, K. G. Sullivan, D. G. Hall, *J. Opt. Soc. Am. B* **10**, 391 (1993).
5. J. L. Jewell, J. P. Harbison, A. Scherer, Y. H. Lee, L. T. Florez, *IEEE J. Quantum Electron.* **27**, 1332 (1991).
6. S. L. McCall, A. F. J. Levi, R. E. Slusher, S. J. Pearton, R. A. Logan, *Appl. Phys. Lett.* **60**, 289 (1992).
7. J. D. Joannopoulos, R. D. Meade, J. N. Winn, *Photonic Crystals* (Princeton Univ. Press, Princeton, NJ, 1995).
8. O. Painter, J. Vučković, A. Scherer, *J. Opt. Soc. Am. B* **16**, 275 (1999).
9. Finite-difference time-domain calculations of the spontaneous emission coupling factor (β) of the defect cavity show that ~65% of the emission is captured by the defect mode when the emission linewidth is as large as 12% of the peak wavelength (J. Vučković, O. Painter, Y. Xu, A. Yariv, A. Scherer, *IEEE J. Quantum ELectron.*, in press).
10. H. Yokoyama, *Science* **256**, 66 (1992).
11. T. Yoshie, C. C. Cheng, A. Scherer, in *1998 IEEE 16th International Semiconductor Laser Conference*, Nara, Japan, 5 to 10 October 1998 (IEEE, Piscataway, NJ, 1998).
12. T. Baba and T. Matsuzaki, *Jpn. J. Appl. Phys. 1* **35**, 1348 (1996).
13. Y. Zhou *et al.*, *IEEE Photonics Technol. Lett.* **4**, 1315 (1992).
14. I. Kim, D. G. Chang, P. D. Dapkus, *J. Cryst. Growth* **119**, 138 (1988).
15. P. R. Villeneuve, S. Fan, J. D. Joannopoulos, *Phys. Rev. B* **54**, 7837 (1996).
16. P. R. Villeneuve, S. Fan, S. G. Johnson, J. D. Joannopoulos, *IEE Proc. Optoelectron.* **145**, 384 (1998).
17. R. Coccioloi, M. Boroditsky, K. W. Kim, Y. Rahmat-Samii, E. Yablonovitch, *ibid.*, p. 391.
18. R. K. Lee, O. J. Painter, B. Kitzke, A. Scherer, A. Yariv, *Electron. Lett.* **35**, 569 (1999).
19. A. F. J. Levi, S. L. McCall, S. J. Pearton, R. A. Logan, *ibid.* **29**, 1666 (1993).
20. S. M. K. Thiyagarajan, *ibid.* **34**, 2333 (1998).

21. O.J.P. and R.K.L. acknowledge support from the Natural Sciences and Engineering Research Council of Canada. This work was supported by the U.S. Army Research Office (contract DAAH04-96-1-0389) and NSF (contract ECS-9632937).

24 February 1999; accepted 10 May 1999